Lithium Ion Battery Materials as Tunable, Redox Non-Innocent Catalyst Supports

Alon Chapovetsky[1], Ryan Witzke[1], Robert M. Kennedy[1], Evan C. Wegener[1], Fulya Dogan[1], Prajay Patel[1], Magali Ferrandon[1], Jens Niklas[1], Oleg G. Poluektov[1], Ning Rui[2], Sanjaya D. Senanayake[2], José A. Rodriguez[2], Christopher Johnson[1], Cynthia J. Jenks,[1] A. Jeremy Kropf[1], Cong Liu[1], Massimiliano Delferro[1,*], and David M. Kaphan[1,*]

[1]Chemical Sciences and Engineering Division, Argonne National Laboratory, Lemont, Illinois 60439, United States
[2]Chemistry Division, Brookhaven National Laboratory, Upton, New York 11973, United States

Abstract

The development of general strategies for the electronic tuning of a catalyst's active site is an ongoing challenge in heterogeneous catalysis. To this end we report the application of cathode and anode materials as redox non-innocent catalyst supports that can be continuously modulated as a function of lithium intercalation. A zero valent nickel complex was oxidatively grafted onto the surface of lithium manganese oxide ($Li_xMn_2O_4$) to yield single-sites of Ni^{2+} ($Ni/Li_xMn_2O_4$). Its activity for olefin hydrogenation was found to be a function of the redox state of the support material, with the most lithiated variant showing the most activity. X-ray absorption, X-ray photoelectron, solid-state nuclear magnetic resonance and electron paramagnetic resonance spectroscopies, and electron microscopy techniques established the nature of the nickel species on $Li_xMn_2O_4$. Catalyst control through support redox non-innocence was extended to an organotantalum complex on lithium titanium oxide (Li_xTiO_2), demonstrating the generality of this phenomenon.

The discovery of general strategies for the stereoelectronic modulation of active site structure toward tunable activity and selectivity is a grand and ongoing challenge in heterogeneous catalysis.[1-3] Industrial processes require robust catalysts that can withstand continuous processing and separation on a large scale; for that reason, heterogeneous catalysts have dominated industrial

applications. However, while necessitated by practical considerations, heterogeneous catalysts lack certain attributes that their homogeneous counterparts possess, namely the electronically tunable nature of the supporting organic ligand architecture.[3]

In recent decades, surface organometallic chemistry (SOMC) emerged as a powerful strategy for the development of heterogeneous, single-site, *homogeneous-in-function* catalysts through the chemisorption of molecular precursors onto inorganic support materials.[4, 5] These support materials, most commonly silica (SiO_2) and alumina (Al_2O_3), play a crucial role in stabilizing and site-isolating reactive intermediates on the surface.[6-11] While this strategy has been leveraged to great effect, the chemical properties of the support are seldom employed to modulate catalyst reactivity, despite the fact that the surface occupies the inner-coordination-sphere for single-site catalysts, and therefore plays an intimate role in determining the electronic properties of the catalyst. The treatment of supports as chemically dynamic ligands, as opposed to high-surface-area dispersants would allow for the application of lessons learned from the homogeneous catalysis literature, unlocking unique reactivity. The continuous leveraging of the electronic structure of the support towards the activity of the surface species represents an opportunity for innovation in the design and investigation of heterogenized catalyst systems.[1]

Organic ancillary ligands in molecular catalysts play a major role in determining the reactivity of the metal centers to which they are bound. Their electronic characteristics, as determined by their σ-/π- donor and acceptor properties, have been shown to serve as useful handles for manipulating catalyst activity. Beyond control over the electronics of the metal center, the redox properties of conjugated organic ligands also allow them to play an active role in the reversible storage of electrons during the catalytic process, especially for first-row transition metals. These redox non-innocent ligands facilitate key chemical steps by storing and transferring

electrons, enabling multi-electron redox elementary transformations from metals with energetically inaccessible or filled *d*-orbitals (Figure 1A, left).[12-20]

While heterogeneous supports are often more decoupled from catalytic reactivity compared to supporting ligands in homogeneous catalysis, they can play an important role in determining the properties of a supported catalyst. The dynamic relationship between nanoparticles and reducible support materials is often rationalized by Strong Metal Support Interactions (SMSI).[21, 22] Electronic Metal Support Interactions (EMSI), a subset of SMSI, can be viewed as a heterogeneous analogy to redox non-innocent ligand interactions. In an early example of the phenomenon, Rodriguez and co-workers found that metal-oxide supported nanoparticles offered improved stabilization to reactive intermediates relative to bare platinum.[23] In another example of EMSI, Saeys, Seebauer, and coworkers have shown that the performance of a titania supported Pt nanoparticle catalyst was dependent on the carrier properties of the support, which was inversely proportional to its size.[24-26] Given the ability to modulate their Fermi levels, band structures, and surface potentials, redox non-innocent or EMSI capable supports could facilitate catalytic transformations analogous to their molecular counterparts. Despite the recognition EMSI has gained in the field, there are relatively few examples in which it is actively leveraged to tune catalytic reaction outcomes. While a few examples of SOMC systems on reducible support materials such as titania and ceria exist, the presence of EMSI has not been demonstrated or utilized in those examples (Figure 1A, right).[27-35]

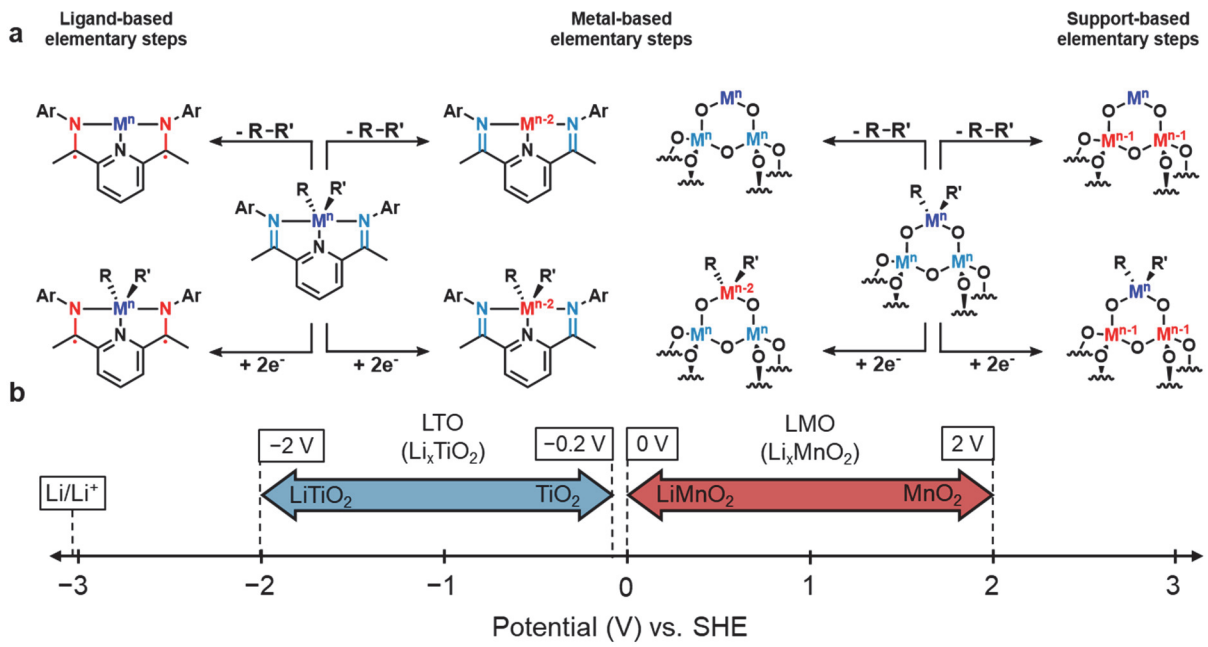

Figure 1. (a) Analogy between redox non-innocent molecular ligands and comparable redox noninnocence of a solid catalyst support. (b) surface potentials achievable by redox tuning of two battery anode/cathode materials, lithium titanium oxide and lithium manganese oxide.

In contrast to traditional support materials such as titania and ceria that can participate in EMSI, lithium ion battery cathode and anode materials such as lithium manganese oxide (LMO, Li_xMnO_2) and lithium titanium oxide (LTO, Li_xTiO_2) are attractive candidates for redox-active supports due to their broad range of available charge states and the ability to tune surface potentials as a function of lithium intercalation (Figure 1B). In this work, the LMO used has the cubic spinel crystal phase which is stoichiometrically defined as $Li_xMn_2O_4$, representing a single phase solubility of chemically tunable Li. Modulating the degree of lithium intercalation affords a series of materials with continuously varying potentials, allowing for the discrete electronic tuning of the surface species, making them ideal for EMSI. Charging the anode material LTO results in a nearly 2 V span of surface potential between the fully reduced $LiTiO_2$ (-2 V vs SHE) and delithiated titanium oxide (-0.2 V vs SHE). Likewise, stoichiometric lithiation of LMO spans a 2 V range from $LiMnO_2$ (0 V vs SHE) to MnO_2 (2 V vs SHE).[36] Thus, in theory, the two support materials, span nearly 4 V of surface potential

is accessible, which may imbue previously inaccessible levels of catalyst tunability. Herein, we report a series of single-site nickel catalysts grafted on lithiated manganese oxides that exhibit activity as a function of the charge state of the support material. The generality of this phenomenon is demonstrated by extension to a TiO_2 supported organotantalum catalyst that exhibits enhanced reactivity upon lithiation of the support material. This work represents a proof-of-principle for the general strategy of electronic catalyst modulation through continuous chemical modulation of the charge state of the support.

Results and Discussion

Synthesis and Characterization of Ni/Li_xMnO_2. The relatively low density of hydroxyl groups on the surface of LMO complicates traditional SOMC grafting techniques such as protonolysis and condensation. However, the oxidizing nature of the support opens the possibility of an orthogonal mechanism of chemisorption by abstraction of one or more electrons from a low-valent molecular precursor, leaving the metal active site coulombically and/or covalently bound to the surface. Similar oxidative chemisorption involving redox interactions have previously been reported in the grafting of in situ generated Au(0) and Ag(0) on MnO_2 nano materials, as well as in the chemisorption of molecular Ru(0) phosphine complex by oxidative addition to the O-H bond of a silica surface hydroxyl group.[37-39] To evaluate the viability of this approach, a solution of bis(cyclooctadiene)nickel(0) ($Ni(COD)_2$) was added to a suspension of $LiMn_2O_4$, which was mechanically agitated and monitored by ^{1}H NMR spectroscopy over the course of 48 hours (Figure 2B). The concentration of $Ni(COD)_2$ decreased sharply upon exposure to the LMO surface, with concomitant appearance of between one and two equivalents of cyclooctadiene (*vide infra*). After the first hour, the concentration of $Ni(COD)_2$ decreased only marginally, and saturation was achieved after 24 hours (Figure S2). In contrast, when $Ni(COD)_2$ was exposed to silica partially

dehydroxylated under vacuum at 700 °C no significant chemisorption of nickel was observed, underscoring the role of the oxidizing surface in the grafting reaction (Figure S3,S4).

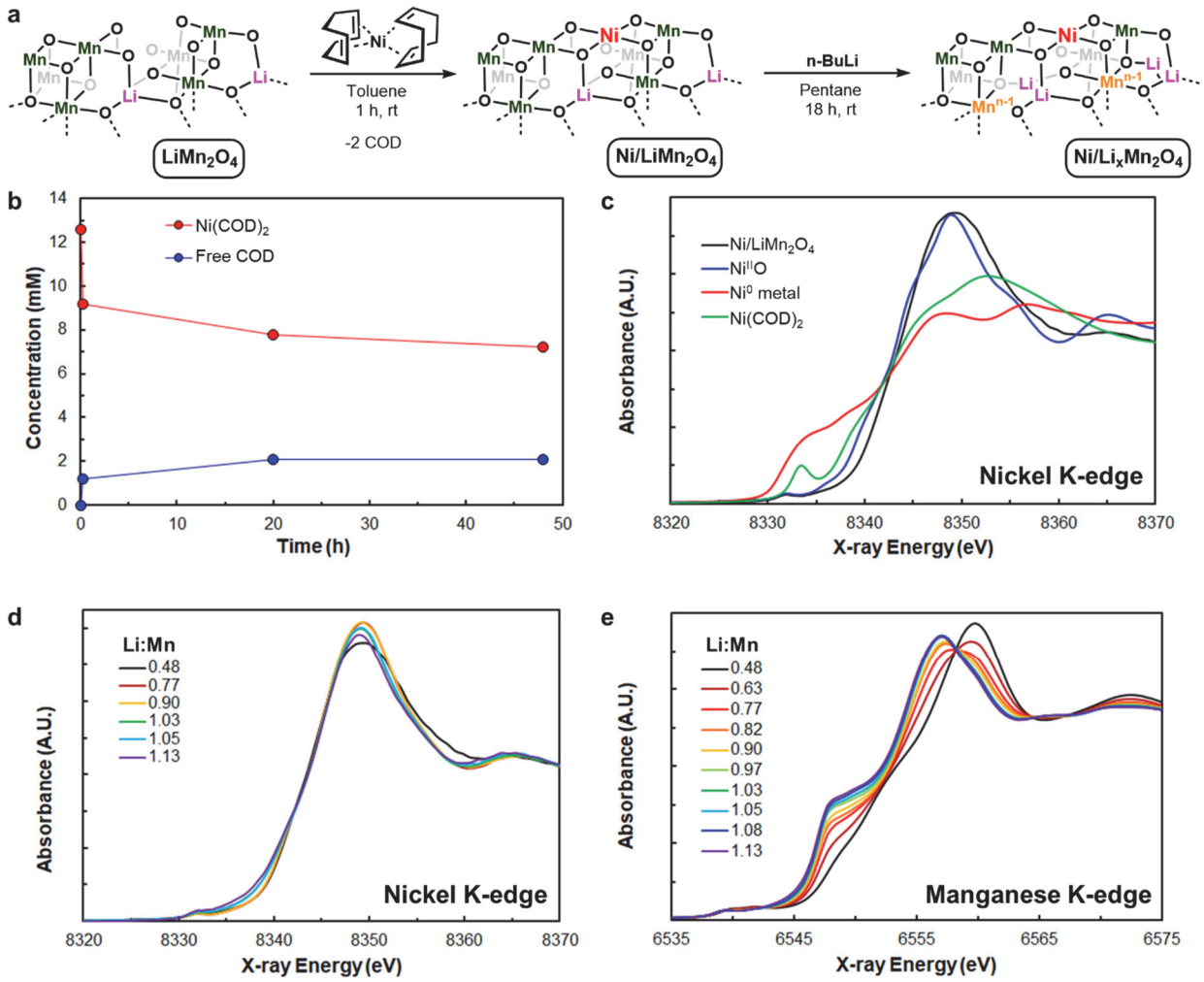

Figure 2. (A) The oxidative grafting of $Ni(COD)_2$ onto $LiMn_2O_4$ to make **Ni/LiMn$_2$O$_4$**, and its reduction to make **Ni/Li$_x$Mn$_2$O$_4$** (X = 0.96 – 2.26). Lithiation biproducts include butane and butenes. (B) reaction profile for the chemisorption of $Ni(COD)_2$ onto $LiMn_2O_4$, (C) XANES spectra of **Ni/Li$_{0.96}$Mn$_2$O$_4$**, and some nickel standards, and (D) Ni and (E) Mn XANES spectra of the variably reduced material **Ni/Li$_x$Mn$_2$O$_4$** (X = 0.96 – 2.26). The relative positions of the edges and white lines support the conclusion that nickel retains its oxidation state while manganese is reduced to Mn +3 from Mn +4/+3.

Preparative scale chemisorption resulted in the isolation of the metallated LMO precatalyst (**Ni/LiMn$_2$O$_4$**, 0.50 wt % Ni by ICP-MS). Analysis of the isolated material by diffuse reflectance

124 infrared spectroscopy (DRIFT) and thermogravimetric analysis (TGA-MS) support the absence of
125 COD ligands on the surface, suggesting that the residual COD was physisorbed and removed upon
126 isolation (Figure S5). High-angle annular dark field scanning transmission electron microscopy
127 (HAADF-STEM) images (Figure 3A, S7A), along with Energy-dispersive X-ray spectroscopy (EDS)
128 maps of **Ni/LiMn$_2$O$_4$** (Figure 3B-D, S7B-D) corroborate the dispersity of nickel on the surface with
129 no agglomeration to clusters or nanoparticles. Lithiation of **Ni/LiMn$_2$O$_4$** was performed via the
130 addition of *n*-butyllithium (2.5 M in pentane) to a suspension of the manganese oxide material in
131 pentane at -36 °C followed by agitation at 22 °C over the course of 18 hours (Figure 1A). Variation of
132 the *n*-butyllithium stoichiometry resulted in a series of reduced materials with lithium to
133 manganese ratios ranging from 0.48 to 1.12 (Table S5). HAADF-STEM and EDS maps of the fully
134 reduced material, **Ni/Li$_{2.26}$Mn$_2$O$_4$**, show that upon reduction nickel remains site-isolated and
135 dispersed on the surface of the support (Figure 3E-H, S8A-D). Electron paramagnetic resonance
136 (EPR) spectroscopy of **Ni/LiMn$_2$O$_4$** and **Ni/Li$_{2.26}$Mn$_2$O$_4$** showed similar spectra consisting of a
137 broad signal centered at g = 2 (≈ 340mT), typical of Mn^{3+}/Mn^{4+} in an exchange coupled system
138 (Figure S9).

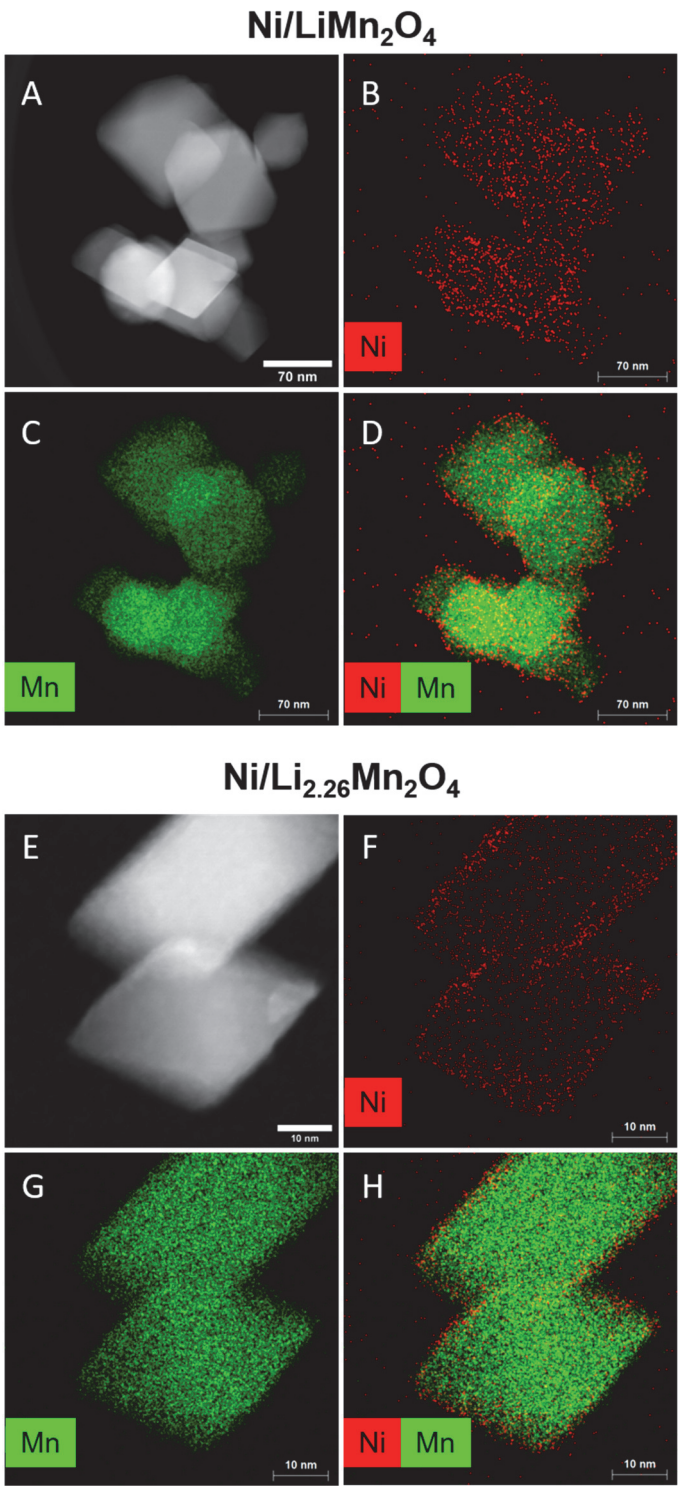

Figure 3. TEM images and EDS maps for **Ni/Li$_{0.96}$Mn$_2$O$_4$** (left, panels A-D) and **Ni/Li$_{2.26}$Mn$_2$O$_4$** (right, panels E-H). The TEM images show the persistence of the morphology of the manganese oxide particles after reduction while the EDS maps confirm that regardless of the extent of lithiation, nickel is dispersed, and site isolated on the surface of the support.

X-ray absorption spectroscopy (XAS) and X-ray Photoelectron Spectroscopy (XPS) were used to determine the oxidation state of nickel on the surface. The pre-edge and white line features (8331.6 and 8349.2 eV, respectively) in the XANES of **Ni/LiMn$_2$O$_4$** were consistent with nickel in the +2-oxidation state (Figure 2C).[40] Similarly, the XPS of **Ni/LiMn$_2$O$_4$** exhibited two sets of peaks with binding energies of 855.2 and 873.1 eV corresponding to the $2p_{3/2}$ and $2p_{1/2}$ levels, respectively, consistent with a Ni^{2+} ion in an oxygen rich environment distinct from nickel oxide (853.5 eV) and opposed to nickel metal (852.5 eV) (SI, Figure S10. Both XAS and XPS confirm that nickel is oxidized upon chemisorption, consistent with an oxidative grafting reaction between Ni(COD)$_2$ and LiMn$_2$O$_4$. The Ni-XANES of the variably reduced materials exhibit a very small difference in pre-edge peak and edge energies relative to the parent **Ni/LiMn$_2$O$_4$**. The white line narrows and a shoulder on the high energy side of the white line becomes a valley. As the extent of lithiation increases, a small increase in the rising edge is observed, possibly indicative of a reduced minor species or the presence of a more electron rich environment. Alternatively, the increase in the rising edge intensity and the decrease in the white line may indicate lower Ni site symmetry. These differences notwithstanding, the majority of the nickel sites remain in the +2 oxidation state regardless of the stoichiometry of the *n*-butyllithium reductant added (Figure 2D). In contrast, the Mn XANES of **Ni/LiMn$_2$O$_4$** underwent a shift in the edge to lower energy and growth of the pre-edge feature at 6545 eV upon addition of n-butyllithium, consistent with a full conversion to manganese 3+ (Figure 2E).[41, 42] Fitting of the Ni-EXAFS data revealed an oxygen-rich environment with 5-6 nearest neighbors and the presence of a Mn second nearest neighbor environment. Lon-range order beyond the second nearest neighbor, such as seen in NiO, LiMn$_2$O$_4$, or LiMnO$_2$ was not observed, ruling out the formation of large nickel oxide nanoparticles (Figure S11-13). However, the Ni local structure changes after reduction to increase the Ni-O bond length and the Ni-Mn path length by an average of 0.023 Å and 0.046 Å, respectively. Finally, the ^{6}Li solid state NMR spectra

of **Ni/LiMn$_2$O$_4$** and **Ni/Li$_{2.26}$Mn$_2$O$_4$** were consistent with a reduction of the average manganese oxidation state from +3.5 to +3 concomitant with a structural rearrangement from the spinel LiMn$_2$O$_4$ to a tetragonal Li$_2$Mn$_2$O$_4$ which was further corroborated via X-ray powder diffraction (Figure S15).

Reactivity of Ni/Li$_x$Mn$_2$O$_4$. The hydrogenation of alkenes was chosen as a model reaction to test the activity of the variably reduced materials (Figure 4A). It was hypothesized that reduction of the support would increase electron density at the Ni active site, facilitating the bond activations involved in the hydrogenation process. Activity was probed using ^{1}H NMR spectroscopy with 0.1 M cyclohexene solution in C$_6$D$_6$ (1 mol% Ni) and approximately 4 atm H$_2$. **Ni/LiMn$_2$O$_4$** was not active towards the hydrogenation of olefins regardless of the material loading or reaction conditions (Figure S16). However, hydrogenation activity was observed upon lithiation at a Li:Mn ratio of 0.90 and above (Figure S17). Control experiments with the nickel-free support did not result in hydrogenation, and filtration of the reaction mixture at partial conversion resulted in a solution that was not active for olefin hydrogenation, ruling out the desorption of a catalytically active species (Figure S18,19). A series of ethereal and aliphatic olefins and alkynes were hydrogenated efficiently by **Ni/Li$_{2.26}$Mn$_2$O$_4$**, however, more polar functional groups were not tolerated (Table S6).

Kinetic measurements on the full range of reduced materials were performed by monitoring the change in hydrogen pressure over time of a toluene suspension of cyclohexene (0.1 M) and **Ni/Li$_x$Mn$_2$O$_4$** (1 mol% Ni) in a batch reactor pressurized with roughly 95 PSI-A of H$_2$ (Figure 4A, S15). No measurable hydrogenation was observed for **Ni/Li$_x$Mn$_2$O$_4$** materials with Li:Mn ratios of up to 0.82. However, an onset of activity was observed for the material with Li:Mn ratio of 0.90, and catalytic rates increased monotonically with the degree of further support lithiation (Figures S22-27, Tables S6). The nickel and manganese XANES and EXAFS spectra of **Ni/Li$_{2.06}$Mn$_2$O$_4$** post

catalysis were similar to the pristine material, suggesting that a significant structural rearrangement does not occur under reaction conditions (Figure S29). The correlation between the catalytic rates and the Li:Mn ratios of **Ni/Li$_x$Mn$_2$O$_4$** suggests that lithiation plays a critical role in the generation of catalytically active nickel species and stabilization of reactive intermediates.

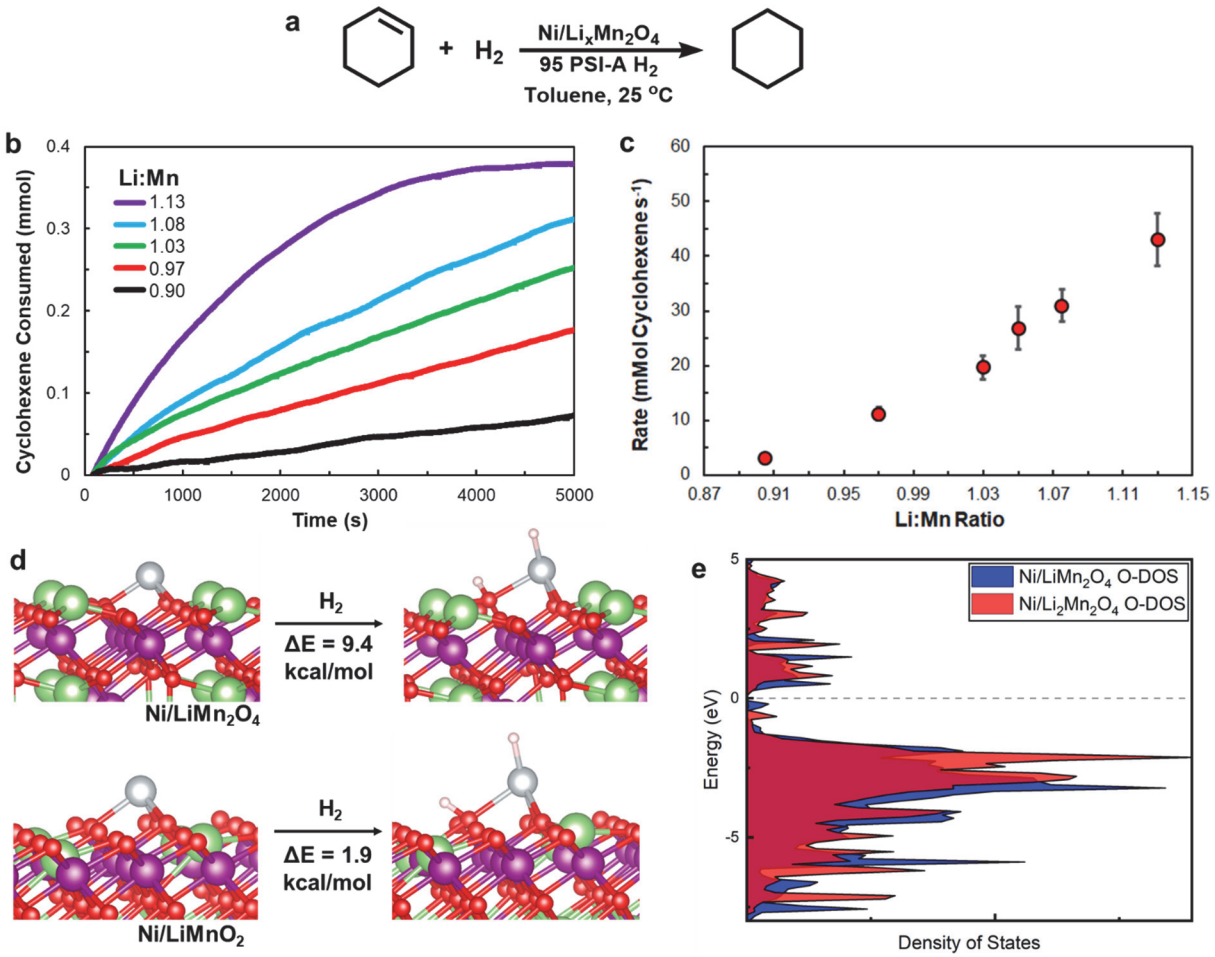

Figure 4. (A) Reaction scheme and conditions for the hydrogenation of cyclohexene to cyclohexane. (B) Reaction profile for the hydrogenation of cyclohexene with **Ni/Li$_x$Mn$_2$O$_4$** (X = 0.9 – 1.12) and (C) Experimental catalytic rate constants (mmol olefin per s^{-1}, normalized to mol nickel), as a function of the lithium content for the screened materials measured in the presence of 0.1 M cyclohexene under 95 PSI-A of H_2. Each measurement was performed in triplicate and materials were compared within the same batch of **Ni/Li$_x$Mn$_2$O$_4$** to eliminate any batch-to-batch variability. Vertical error bars represent one standard deviation. (D) DFT optimized structure of **Ni/LiMn$_2$O$_4$** and **Ni/LiMnO$_2$**, and thermodynamics of their activation of H_2. (E) Oxygen p-orbital density of states (DOS) for oxygen adjacent to the nickel active site, reflecting an increase in filled states below the Fermi level.

To gain insight into the range of possible nickel coordination environments and to further understand how surface lithiation might impact the reactivity of the nickel center, a series of active site models were computationally investigated. The (111) facet was chosen for study as it is known to exhibit the highest stability among all $LiMn_2O_4$ facets.[43, 44] Structures where nickel occupied a manganese vacancy, a lithium vacancy and a tripodal coordination mode on an oxygen termination were calculated for both the $LiMn_2O_4$ and the $LiMnO_2$ surface (Table S8). The nickel in the tripodal surface site and the lithium vacancy both showed a small change in magnetization upon lithiation, which is associated with a slight increase in electron occupancy in the *d*-orbital, while the magnetization of the nickel in the manganese vacancy was unchanged. Further insight into how lithiation might influence the reactivity of these sites was obtained by investigating the thermodynamics of dihydrogen activation by both oxidative addition and heterolytic activation across the Ni-O bond (Table S9). Homolytic H_2 activation as found uniformly to be significantly higher in energy than the heterolytic activation, and so further investigation focused on the latter mechanism. While heterolytic H_2 activation was roughly isoenergetic for the lithium vacancy site, lithiation was found to lower the energy of bond activation by 7.5 kcal/mol for the nickel in a tripodal surface site (ΔG = 9.4 kcal/mol and 1.9 kcal/mol respectively, Figure 4D). As this bond activation is oxidizing with respect to the surface, it is logical that increased electron density at the active site upon lithiation would lower the energy of the transformation. Indeed, while the nickel site undergoes only a minor change in magnetization, the oxygen atom that participates in the heterolytic bond activation undergoes a much larger change in magnetization upon lithiation of the support (Table S10), reflecting a significant buildup of partial charge at the oxygen atoms on the surface, rendering them more reactive toward heterolytic bond activation. This increase in

electron density is further demonstrated by the appearance of a significant increase in the density of states for the oxygen p-orbitals just below the Fermi level of the material (Figure 4E).

Extension to Anode Material Lithium Titanium Oxide.

In order to evaluate the generality of support lithiation as a strategy for modulation of catalyst reactivity, an analogous system was targeted on the reducing anode material lithium titanium oxide. Tris(neopentyl)tantalum dichloride ($Ta(CH_2C(CH_3)_3)_3Cl_2$) was chemisorbed on anatase TiO_2 nanoparticles, which resulted in the release of two equivalents of neopentane per tantalum complex deposited on the surface based on *in situ* ^{1}H NMR spectroscopic monitoring of the grafting reaction, suggesting a bipodal complex on the surface.[45] The chemisorption reached saturation with a loading of 0.8 wt % of Ta, affording **Ta/TiO$_2$** (Figures 5A, S30). This material was reduced with an excess of lithium naphthalide (LiNap), to afford **Ta/Li$_x$TiO$_2$** (0.458 wt% Ta, x = 0.77). It was not clear if the Ta site would also be reduced upon exposure to Li napthalide. To evaluate this, **Ta/TiO$_2$** and **Ta/Li$_x$TiO$_2$** were examined by XAS. Ti K-edge XANES displayed a shift in both the absorption edge and the pre-edge features to lower energy upon lithiation, as well as a decrease in white line intensity, consistent with a decrease in the average oxidation state of titanium (Figure 5D). In contrast, the Ta XANES of **Ta/TiO$_2$** and **Ta/Li$_x$TiO$_2$** exhibited qualitatively similar edge energies and very little change in the magnitude of the white line, suggesting that the oxidation state of Ta, +5, remains constant upon the lithiation of the titania surface (Figure 5C).

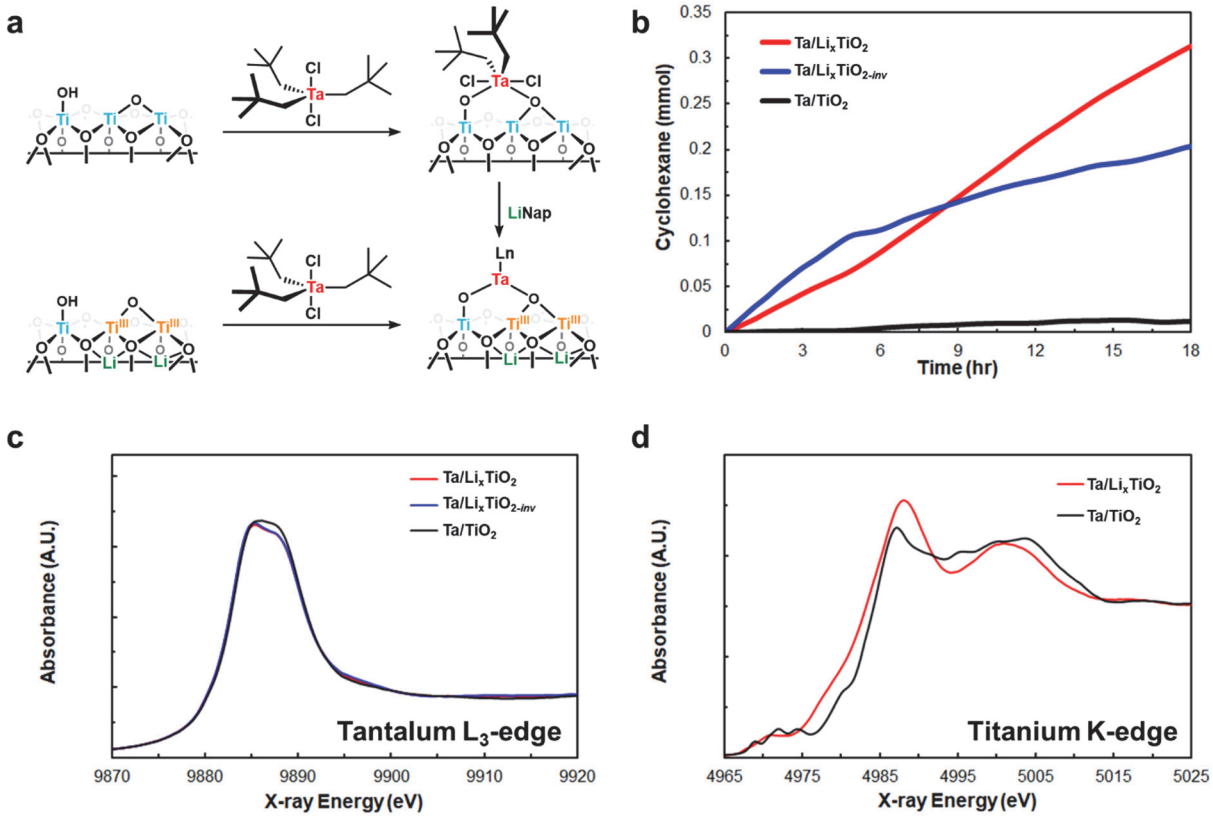

Figure 5. The grafting and lithiation of tris(neopentyl)tantalum on titania to make **Ta/Li$_x$TiO$_2$** and **Ta/Li$_x$TiO$_{2\text{-}inv}$**. (B) Reaction profile for the hydrogenation of cyclohexene with **Ta/Li$_x$TiO$_2$**, **Ta/Li$_x$-TiO$_{2\text{-}inv}$**, and **Ta/TiO$_2$**. (C) tantalum and (D) titanium XANES spectra for the materials. The relative positions of the edges and white lines support that conclusion that tantalum retains its oxidation state while titanium is reduced upon lithiation.

The activity of the reduced and unreduced materials for the hydrogenation of cyclohexene was evaluated in a batch reactor under conditions described above (for further detail, see SI Pages S29-S31). No measurable activity was observed for the unreduced **Ta/TiO$_2$**, while **Ta/Li$_x$TiO$_2$** catalyzed the reaction with a half-life of approximately 9 hours, and an induction period was observed, consistent with the formation of a secondary active species (Figure 5B). To further test the hypothesis that the activity of **Ta/Li$_x$TiO$_2$** stems from the charge state of the support as opposed to direct reduction of the surface species, the tantalum precursor was chemisorbed onto the pre-lithiated support to afford **Ta/Li$_x$TiO$_{2\text{-}inv}$** (*inv* denoting the inverse order of metalation and lithiation) (Figure 5A). The Ta XANES of **Ta/Li$_x$TiO$_{2\text{-}inv}$**, like that of **Ta/Li$_x$TiO$_2$**, did not display a

shift in edge energy, suggesting that the +5-oxidation state of Ta is maintained regardless of the order of metalation and lithiation (Figure 5C). **Ta/Li$_x$TiO$_{2\text{-}inv}$** was found to effect the hydrogenation of cyclohexene at a similar rate to **Ta/Li$_x$TiO$_2$**, further supporting the role of electronic communication between the support and the active supported catalytic complex. Interestingly, the kinetic profile obtained from the hydrogenation of cyclohexene using **Ta/Li$_x$TiO$_{2\text{-}inv}$** did not display an induction period, suggesting that the species generated by direct grafting on the pre-reduced surface may be more similar to the active species than that generated by chemisorption followed by reduction. A parallel can be drawn between the Ta/LTO system and the Ni/LMO system. In both systems, the catalyst activity can be modulated as a function of lithium intercalation, and while the bulk support material undergoes reduction upon lithiation, minimal redox changes are observed at the supported active sites.

This work describes a general approach to the modulation of the activity of a single-site heterogeneous catalyst system by a continuously tunable variable, the reduction and intercalation of lithium ions into the matrix of the support material. The series of **Ni/Li$_x$Mn$_2$O$_4$** (X = 0.96 – 2.26) materials is an example of a system in which the support acts as a redox active ligand and its electronic properties are used to control its catalytic performance. The extension of these results to the **Ta/Li$_x$TiO$_2$** system demonstrates the generality of this phenomenon. Notably, for both the Ni/LMO and Ta/LTO systems, the redox modulation in the support, consistent with the facile electronic communication between support and active site, and possible redox non-innocent behavior of the support throughout the catalytic cycle. The utilization of this new orthogonal axis to modulate catalytic outcomes represents a new frontier at the interface of organometallics, catalysis, and material science. Further leveraging the "redox non-innocent" properties of cathode materials towards catalysis is expected to result in novel systems capable of facilitating difficult transformations through innovative mechanisms. Support materials with appropriate fermi levels

and band structures could store multiple equivalents of electrons, allowing for complex, multi-electron transformations such as N_2 and CO_2 reduction. Work in this area will draw on the wealth of knowledge surrounding lithium intercalation derived from the development of Li-ion battery cathode and anode materials. Future efforts will concentrate on the expansion of the scope of the reactivity of the current materials, and elucidation of the electron storage and transfer dynamics between the bulk and the surface.

Funding:

Work at Argonne National Laboratory was supported by the U.S. Department of Energy (DOE), Office of Basic Energy Sciences, Division of Chemical Sciences, Geosciences, and Biosciences, Catalysis Science Program under contract No. DE-AC-02-06CH11357. All DFT and XANES calculations were performed using the computational resources at provided by the Laboratory Computing Resource Center (LCRC) at Argonne National Laboratory (ANL). Use of the Advanced Photon Source is supported by the U.S. Department of Energy, Office of Science, and Office of the Basic Energy Sciences, under Contract No. DEAC02–06CH11357. MRCAT operations are supported by the Department of Energy and the MRCAT member institutions. Use of the TEM at the Center for Nanoscale Materials at Argonne National Laboratory is supported by the U.S. Department of Energy, Office of Science, Office of Basic Energy Sciences, under contract No. DE-AC-02-06CH11357.Work by Chris Johnson was supported as part of the Center for Electrochemical Energy Science (CEES), an Energy Frontier Research Center funded by the U.S. Department of Energy, Office of Science, Basic Energy Sciences. The experimental studies carried out at Brookhaven National Laboratory (AP-XPS) were supported by the US Department of Energy under contract number DE-SC0012704. F.D. acknowledges support from the Vehicle Technologies Office at the U.S. Department of Energy, Energy Efficiency and Renewable Energy. The EPR work (O.G.P, J.N.) was supported by the U.S. Department of Energy (DOE), Office of Basic Energy Sciences, Division of Chemical Sciences, Geosciences, and Biosciences, under Contract no. DE-AC-02-06CH11357.

Notes

The authors declare the following competing financial interest(s): A patent application partially based on this work has been filed (US Patent Application 17/077,630).

Acknowledgements:

We thank the Carus Group for the generous donation of high surface area MnO_2.

1. Witzke, R. J.; Chapovetsky, A.; Conley, M. P.; Kaphan, D. M.; Delferro, M., Nontraditional Catalyst Supports in Surface Organometallic Chemistry. *ACS Catal.* **2020**, *10*, 11822-11840.
2. Copéret, C.; Comas-Vives, A.; Conley, M. P.; Estes, D.; Nunez-Zarur, F.; Fedorov, A.; Mougel, V.; Nagae, H.; Zhizhko, P. A., Surface Organometallic and Coordination Chemistry towards Single-Site Heterogeneous Catalysts: Strategies, Methods, Structures, and Activities. *Chem. Rev.* **2016,** *116*, 323-421.
3. Copéret, C.; Allouche, F.; Chan, K. W.; Conley, M. P.; Delley, M. F.; Fedorov, A.; Moroz, I. B.; Mougel, V.; Pucino, M.; Searles, K.; Yamamoto, K.; Zhizhko, P. A., Bridging the Gap between Industrial and Well-Defined Supported Catalysts. *Angew. Chem., Int. Ed.* **2018,** *57*, 6398-6440.
4. Copéret, C.; Fedorov, A.; Zhizhko, P. A., Surface Organometallic Chemistry: Paving the Way Beyond Well-Defined Supported Organometallics and Single-Site Catalysis. *Catal. Lett.* **2017,** *147*, 2247-2259.
5. Samantaray, M. K.; D'Elia, V.; Pump, E.; Falivene, L.; Harb, M.; Ould Chikh, S.; Cavallo, L.; Basset, J. M., The Comparison between Single Atom Catalysis and Surface Organometallic Catalysis. *Chem. Rev.* **2020,** *120*, 734-813.
6. Chan, K. W.; Mance, D.; Safonova, O. V.; Copéret, C., Well-Defined Silica-Supported Tungsten(IV)–Oxo Complex: Olefin Metathesis Activity, Initiation, and Role of Brønsted Acid Sites. *J. Am. Chem. Soc.* **2019,** *141*, 18286-18292.
7. Lebedev, D.; Pineda-Galvan, Y.; Tokimaru, Y.; Fedorov, A.; Kaeffer, N.; Copéret, C.; Pushkar, Y., The Key RuV=O Intermediate of Site-Isolated Mononuclear Water Oxidation Catalyst Detected by in Situ X-ray Absorption Spectroscopy. *J. Am. Chem. Soc.* **2018,** *140*, 451-458.
8. Chen, Y.; Callens, E.; Abou-Hamad, E.; Merle, N.; White, A. J.; Taoufik, M.; Coperet, C.; Le Roux, E.; Basset, J. M., [(≡SiO)TaVCl$_2$Me$_2$]: A Well-Defined Silica-Supported Tantalum(V) Surface Complex as Catalyst Precursor for the Selective Cocatalyst-Free Trimerization of Ethylene. *Angew. Chem., Int. Ed.* **2012,** *51*, 11886-11889.
9. Hamieh, A.; Chen, Y.; Abdel-Azeim, S.; Abou-hamad, E.; Goh, S.; Samantaray, M.; Dey, R.; Cavallo, L.; Basset, J. M., Well-Defined Surface Species [(≡Si–O–)W(═O)Me$_3$] Prepared by Direct Methylation of [(≡Si–O–)W(═O)Cl$_3$], a Catalyst for Cycloalkane Metathesis and Transformation of Ethylene to Propylene. *ACS Catal.* **2015,** *5*, 2164-2171.
10. Chen, Y.; Abou-Hamad, E.; Hamieh, A.; Hamzaoui, B.; Emsley, L.; Basset, J. M., Alkane Metathesis with the Tantalum Methylidene [(≡SiO)Ta(═CH2)Me$_2$]/[(≡SiO)$_2$Ta(═CH$_2$)Me] Generated from Well-Defined Surface Organometallic Complex [(≡SiO)$_{TaVMe4}$]. *J. Am. Chem. Soc.* **2015,** *137*, 588-591.
11. Chapovetsky, A.; Langeslay, R. R.; Celik, G.; Perras, F. A.; Pruski, M.; Ferrandon, M. S.; Wegener, E. C.; Kim, H.; Dogan, F.; Wen, J.; Khetrapal, N.; Sharma, P.; White, J.; Kropf, A. J.; Sattelberger, A. P.; Kaphan, D. M.; Delferro, M., Activation of Low-Valent, Multiply M–M Bonded Group VI Dimers toward Catalytic Olefin Metathesis via Surface Organometallic Chemistry. *Organometallics* **2020,** *39*, 1035-1045.
12. Khan, F. F.; Chowdhury, A. D.; Lahiri, G. K., Bond Activations Assisted by Redox Active Ligand Scaffolds. *Eur. J. Inorg. Chem.* **2020,** *2020*, 1138-1146.
13. Singh, B.; Indra, A., Role of redox active and redox non-innocent ligands in water splitting. *Inorg. Chim. Acta* **2020,** *506*, 119440-119440.

14. Bullock, R. M.; Chen, J. G.; Gagliardi, L.; Chirik, P. J.; Farha, O. K.; Hendon, C. H.; Jones, C. W.; Keith, J. A.; Klosin, J.; Minteer, S. D.; Morris, R. H.; Radosevich, A. T.; Rauchfuss, T. B.; Strotman, N. A.; Vojvodic, A.; Ward, T. R.; Yang, J. Y.; Surendranath, Y., Using nature's blueprint to expand catalysis with Earth-abundant metals. *Science* **2020,** *369* , 1-10.
15. Hojilla Atienza, C. C.; Milsmann, C.; Semproni, S. P.; Turner, Z. R.; Chirik, P. J., Reversible Carbon–Carbon Bond Formation Induced by Oxidation and Reduction at a Redox-Active Cobalt Complex. *Inorg. Chem.* **2013,** *52*, 5403-5417.
16. Darmon, J. M.; Stieber, S. C. E.; Sylvester, K. T.; Fernández, I.; Lobkovsky, E.; Semproni, S. P.; Bill, E.; Wieghardt, K.; DeBeer, S.; Chirik, P. J., Oxidative Addition of Carbon–Carbon Bonds with a Redox-Active Bis(imino)pyridine Iron Complex. *J. Am. Chem. Soc.* **2012,** *134* , 17125-17137.
17. Tondreau, A. M.; Milsmann, C.; Patrick, A. D.; Hoyt, H. M.; Lobkovsky, E.; Wieghardt, K.; Chirik, P. J., Synthesis and Electronic Structure of Cationic, Neutral, and Anionic Bis(imino)pyridine Iron Alkyl Complexes: Evaluation of Redox Activity in Single-Component Ethylene Polymerization Catalysts. *J. Am. Chem. Soc.* **2010,** *132* , 15046-15059.
18. Bouwkamp, M. W.; Bowman, A. C.; Lobkovsky, E.; Chirik, P. J., Iron-Catalyzed [2π + 2π] Cycloaddition of α,ω-Dienes: The Importance of Redox-Active Supporting Ligands. *J. Am. Chem. Soc.* **2006,** *128*, 13340-13341.
19. Haneline, M. R.; Heyduk, A. F., C–C Bond-Forming Reductive Elimination from a Zirconium(IV) Redox-Active Ligand Complex. *J. Am. Chem. Soc.* **2006,** *128*, 8410-8411.
20. Blackmore, K. J.; Ziller, J. W.; Heyduk, A. F., "Oxidative Addition" to a Zirconium(IV) Redox-Active Ligand Complex. *Inorg. Chem.* **2005,** *44*, 5559-5561.
21. Yang, Y.; Mims, C. A.; Mei, D. H.; Peden, C. H. F.; Campbell, C. T., Mechanistic studies of methanol synthesis over Cu from $CO/CO_2/H_2/H_2O$ mixtures: The source of C in methanol and the role of water. *J. Catal.* **2013,** *298*, 10-17.
22. van Deelen, T. W.; Hernández Mejía, C.; de Jong, K. P., Control of metal-support interactions in heterogeneous catalysts to enhance activity and selectivity. *Na. Catal.* **2019,** *2*, 955-970.
23. Bruix, A.; Rodriguez, J. A.; Ramírez, P. J.; Senanayake, S. D.; Evans, J.; Park, J. B.; Stacchiola, D.; Liu, P.; Hrbek, J.; Illas, F., A New Type of Strong Metal–Support Interaction and the Production of H_2 through the Transformation of Water on $Pt/CeO_2(111)$ and $Pt/CeO_x/TiO_2(110)$ Catalysts. *J. Am. Chem. Soc.* **2012,** *134*, 8968-8974.
24. Gunasooriya, G. T. K. K.; Seebauer, E. G.; Saeys, M., Ethylene Hydrogenation over Pt/TiO_2: A Charge-Sensitive Reaction. *ACS Catal.* **2017,** *7*, 1966-1970.
25. Ioannides, T.; Verykios, X. E., Charge Transfer in Metal Catalysts Supported on Doped TiO2: A Theoretical Approach Based on Metal–Semiconductor Contact Theory. *J. Catal.* **1996,** *161*, 560-569.
26. Schwab, G. M.; Koller, K., Combined action of metal and semiconductor catalysts. *J. Am. Chem. Soc.* **1968,** *90*, 3078-3080.
27. Iwasawa, Y.; Sato, H., Preparations of TiO_2-Attached Rh Catalysts and Their Catalysis. *Chem. Lett.* **1985**, *4*, 507-510.
28. Jeantelot, G.; Qureshi, M.; Harb, M.; Ould-Chikh, S.; Anjum, D. H.; Abou-Hamad, E.; Aguilar-Tapia, A.; Hazemann, J.-L.; Takanabe, K.; Basset, J.-M., TiO_2-supported Pt single atoms by surface organometallic chemistry for photocatalytic hydrogen evolution. *Phy. Chem. Chem. Phys.* **2019,** *21*, 24429-24440.
29. Grasser, S.; Haeßner, C.; Kohler, K.; Lefebvre, F.; Basset, J. M., Structures of Paramagnetic VIV Amido Complexes Grafted onto Metal Oxide Surfaces: Model Systems for Heterogeneous Vanadium Catalysts. *Phys. Chem. Chem. Phys.* **2003,** *5*, 1906-1911.
30. Dufour, P.; Houtman, C.; Santini, C. C.; Nedez, C.; Basset, J. M.; Hsu, L. Y.; Shore, S. G., Surface Organometallic Chemistry: Reaction of Tris(allyl)rhodium with Surfaces of Silica, Alumina, Titania and Magnesia. *J. Am. Chem. Soc.* **1992,** *114*, 4248-4257.

31. Guzman, J.; Kuba, S.; Fierro-Gonzalez, J.; Gates, B., Formation of Gold Clusters on TiO_2 from Adsorbed $Au(CH_3)_2(C_5H_7O_2)$: Characterization by X-ray Absorption Spectroscopy. *Catal. Lett.* **2004,** *95*, 77-86.
32. Sheehan, S. W.; Thomsen, J. M.; Hintermair, U.; Crabtree, R. H.; Brudvig, G. W.; Schmuttenmaer, C. A., A Molecular Catalyst for Water Oxidation that Binds to Metal Oxide Surfaces. *Nat. Commun.* **2015,** *6*, 6469-6478.
33. Lebedev, D.; Ezhov, R.; Heras-Domingo, J.; Comas-Vives, A.; Kaeffer, N.; Willinger, M.; Solans-Monfort, X.; Huang, X.; Pushkar, Y.; Copéret, C., Atomically Dispersed Iridium on Indium Tin Oxide Efficiently Catalyzes Water Oxidation. *ACS Cent. Sci.* **2020,** *6*, 1189-1198.
34. Fan, L.; Long, J.; Gu, Q.; Huang, H.; Lin, H.; Wang, X., Single-site nickel-grafted anatase TiO_2 for hydrogen production: Toward understanding the nature of visible-light photocatalysis. *J. Catal.* **2014,** *320*, 147-159.
35. Huang, H.; Lin, J.; Zhu, G.; Weng, Y.; Wang, X.; Fu, X.; Long, J., A Long-Lived Mononuclear Cyclopentadienyl Ruthenium Complex Grafted onto Anatase TiO_2 for Efficient CO_2 Photoreduction. *Angew. Chem., Int. Ed.* **2016,** *55*, 8314-8318.
36. Reddy, M. V.; Subba Rao, G. V.; Chowdari, B. V. R., Metal Oxides and Oxysalts as Anode Materials for Li Ion Batteries. *Chem. Rev.* **2013,** *113*, 5364-5457.
37. Xia, D.; Xu, W.; Wang, Y.; Yang, J.; Huang, Y.; Hu, L.; He, C.; Shu, D.; Leung, D. Y. C.; Pang, Z., Enhanced Performance and Conversion Pathway for Catalytic Ozonation of Methyl Mercaptan on Single-Atom Ag Deposited Three-Dimensional Ordered Mesoporous MnO_2. *Environ. Sci. Technol.* **2018,** *52*, 13399-13409.
38. Chen, J.; Yan, D.; Xu, Z.; Chen, X.; Chen, X.; Xu, W.; Jia, H.; Chen, J., A Novel Redox Precipitation to Synthesize Au-Doped α-MnO_2 with High Dispersion toward Low-Temperature Oxidation of Formaldehyde. *Environ. Sci. Technol.* **2018,** *52*, 4728-4737.
39. Kaplan, A. W.; Bergman, R. G., Nitrous Oxide Mediated Synthesis of Monomeric Hydroxoruthenium Complexes. Reactivity of $(DMPE)_2Ru(H)(OH)$ and the Synthesis of a Silica-Bound Ruthenium Complex. *Organometallics* **1998,** *17*, 5072-5085.
40. Tian, Y.; Etschmann, B.; Liu, W.; Borg, S.; Mei, Y.; Testemale, D.; O'Neill, B.; Rae, N.; Sherman, D. M.; Ngothai, Y.; Johannessen, B.; Glover, C.; Brugger, J., Speciation of nickel (II) chloride complexes in hydrothermal fluids: In situ XAS study. *Chem. Geol.* **2012,** *334*, 345-363.
41. Chan, H.-W.; Duh, J.-G.; Lee, J.-F., Valence change by in situ XAS in surface modified $LiMn_2O_4$ for Li-ion battery. *Electrochem. Commun.* **2006,** *8*, 1731-1736.
42. Okumura, T.; Yamaguchi, Y.; Kobayashi, H., X-ray absorption near-edge structures of $LiMn_2O_4$ and $LiNi_{0.5}Mn_{1.5}O_4$ spinel oxides for lithium-ion batteries: the first-principles calculation study. *Phys. Chem. Chem. Phys.* **2016,** *18*, 17827-17830.
43. Warburton, R. E.; Iddir, H.; Curtiss, L. A.; Greeley, J., Thermodynamic Stability of Low- and High-Index Spinel $LiMn_2O_4$ Surface Terminations. *ACS Appl. Mater. Interfaces* **2016,** *8*, 11108-11121.
44. Chen, L.; Warburton, R. E.; Chen, K.-S.; Libera, J. A.; Johnson, C.; Yang, Z.; Hersam, M. C.; Greeley, J. P.; Elam, J. W., Mechanism for Al2O3 Atomic Layer Deposition on $LiMn_2O_4$ from In Situ Measurements and Ab Initio Calculations. *Chem* **2018,** *4*, 2418-2435.
45. Le Roux, E.; Chabanas, M.; Baudouin, A.; de Mallmann, A.; Copéret, C.; Quadrelli, E. A.; Thivolle-Cazat, J.; Basset, J.-M.; Lukens, W.; Lesage, A.; Emsley, L.; Sunley, G. J., Detailed Structural Investigation of the Grafting of $[Ta(CHtBu)(CH_2tBu)_3]$ and $[Cp^*TaMe_4]$ on Silica Partially Dehydroxylated at 700 °C and the Activity of the Grafted Complexes toward Alkane Metathesis. *J. Am. Chem. Soc* **2004,** *126*, 13391-13399.